TRAVELLING-WAVE ANALYSIS OF EXTENDED CAVITY DIODE LASERS

V. TRONCIU[1,*], B. ARAR[2], H. WENZEL[2]

[1]Department of Physics, Technical University of Moldova, Chisinau MD-2004, Republic of Moldova
[2]Ferdinand-Braun-Institut, Leibniz-Institut für Höchstfrequenztechnik, Gustav-Kirchhoff-Str. 4,
12489 Berlin, Germany,
*Corresponding author, Email: *vasile.tronciu@fiz.utm.md*

Abstract. We report results of numerical simulations of the dynamic properties of single-transverse mode diode lasers subject to an external optical feedback provided by a volume holographic Bragg grating. We use the traveling-wave model for the simulation and analysis of the nonlinear dynamics of the considered devices. We show that the numerical results obtained for a sample device are in a good agreement with the experiment. We investigate the influence of relevant device parameters, such as front and rear facet reflectivities and intra-cavity transmission losses on the laser behaviour.

Key words: semiconductor lasers, optical feedback, bifurcation diagram, volume holographic Bragg grating.

1. INTRODUCTION

In the last decade, semiconductor lasers with an external cavity have received considerable attention for application in quantum sensing and coherent optical communication [1–5]. These applications need lasers having a very small spectral linewidth that can be achieved only by a spectrally filtered feedback. Volume holographic Bragg gratings (VHBGs) providing the wavelength selective feedback are most suitable to realize narrow-linewidth, compact and robust external cavity diode lasers (ECDLs). These laser modules were shown to be very reliable for quantum sensing experiments on sounding rockets [6, 7].

Semiconductor lasers under the influence of delayed optical feedback from an external cavity have been investigated extensively during the past two decades. Studies in the literature include the analysis of continuous wave operation, periodic and quasi-periodic pulsations, low frequency fluctuations, and coherent collapse [8]. The simplest method for modeling a semiconductor laser with weak optical feedback is given by the Lang-Kobayashi model [9]. Despite its simplicity, this model gives a reasonable qualitative agreement with experiments and, therefore, provides a good understanding of nonlinear dynamics in many devices. It has successfully been used to get a deep understanding of the stabilization or destabilization of the continuous wave states by different configurations of external feedback [10, 11].

However, the Lang-Kobayshi model fails for devices with strong feedback such as the ECDL presented in [6]. Therefore, in [12] a traveling-wave model was used for a numerical simulation of the nonlinear dynamics of an ECDL emitting at 780 nm similarly to the one presented in [6]. Based on this model, a detailed analysis of the optical modes was performed and a good qualitative agreement with the experiments was found. Based on the travelling-wave model [12], the electro-optical performance of two different designs of the gain chips (straight and bent ridge waveguides) employed in an ECDL emitting at 1064 nm was compared theoretically and experimentally in [13].

In this paper, we numerically investigate the impact of the reflectivity of the front facet of the gain chip and the intra-cavity transmission losses on the dynamical behavior of an ECDL emitting a 871 nm. Narrow linewidth emission at this wavelength is particularly important for the excitation of the $^2S_{1/2} - ^2D_{3/2}$ transition of a single $^{171}Yb^+$ ion optical clock [14].

The paper is structured as follows. In Sec. 2 we describe the laser setup and the traveling wave model. Section 3 presents the results and discussions. Finally, conclusions are given in Sec. 4.

2. LASER MODEL AND EQUATIONS

Figure 1 shows the schematic structure of the micro-integrated ECDL studied in this paper. It consists of a ridge-waveguide (RW) gain chip, an air gap, and a several millimeter long external VHBG. The diode laser chips are based on GaAs/AlGaAs, have an InGaAsP double quantum well as active region and a fundamental-lateral-mode ridge waveguide design. The rear facet of the RW chip and the facets of the VHBG are AR-coated. We mention that the resonator is formed between the front facet (FF) of the gain chip and the VHBG.
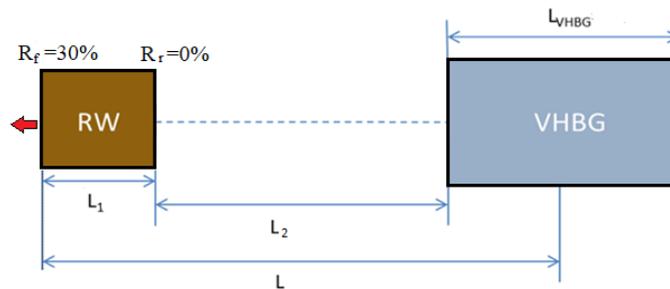

Fig. 1 – A sketch of the setup of an ECDL with external feedback from a VHBG. Front facet reflectivity is $R_f = 0.3$. Rear facet reflectivity is $R_r = 0$.

To model the properties of the ECDL shown in Fig. 1 we use the traveling wave equations

$$\frac{n_{\mathrm{g}}}{c_0}\partial_t E^\pm = \left[\mp\partial_z - i\beta(N,I)\right]E^\pm - i\kappa E^\mp + F_{\mathrm{sp}}^\pm \tag{1}$$

governing the dynamics of the slowly varying complex amplitudes $E^+(z,t)$ and $E^-(z,t)$ of the counter-propagating optical fields. Here c_0 is the speed of light in vacuum, $F_{\mathrm{sp}}^\pm$ is the stochastic contribution of spontaneous emission in the gain section, n_{g} is the group index (different within different parts of the device), and κ is the field coupling coefficient, non-vanishing only in the VHBG. The propagation factor β is given by

$$\beta = \delta_0 - i\frac{\alpha}{2} + k_0\left[\tilde{n}_T(I) + \tilde{n}_N(N)\right] + i\frac{g(N)-\mathcal{D}}{2}, \tag{2}$$

where δ_0 is the detuning from the reference propagation constant, α includes internal losses, $k_0 = 2\pi/\lambda_0$, where λ_0 is the free-space wavelength. Within the gain chip, the propagation factor β contains the functions $\tilde{n}_T(I)$, $\tilde{n}_N(N)$, $g(N)$, and the linear operator $\mathcal{D}$ that is used together with the induced polarization functions $P^\pm(z,t)$ to model the dispersion of the material gain by a Lorentzian approximation [15],

$$\mathcal{D}E^\pm = \overline{g}(E^\pm - P^\pm),\ \partial_t P^\pm = \overline{\gamma}(E^\pm - P^\pm) + i\overline{\omega}P^\pm, \tag{3}$$

where $\overline{g}$, $\overline{\omega}$, and $2\overline{\gamma}$ are the amplitude, the relative central frequency, and the full width at the half maximum of this Lorentzian, respectively. The function $\tilde{n}_T(I)$ describes the dependence of the refractive index on the heating induced by the injection current I [16],

$$\tilde{n}_T(I) = c_T I. \tag{4}$$

The functions $g(N)$ and $\tilde{n}_N(N)$ are given by

$$g(N) = \Gamma g' N_{\mathrm{tr}} \ln\left(\frac{N}{N_{\mathrm{tr}}}\right),\ \tilde{n}_N(N) = \tilde{n}_0 + \frac{\alpha_{\mathrm{H}}\Gamma g'\sqrt{N N_{\mathrm{tr}}}}{k_0}, \tag{5}$$

where Γ is the confinement factor, g' is the prefactor governing the dependence of the gain on the carrier density, $\tilde{n}_0$ is the refractive index offset, and α_{H} is a prefactor governing the dependence of the index on the carrier density. For carrier densities varying only within a small range not too far from N_{tr}, these two nonlinear functions can be efficiently replaced by linear ones:

$$g(N) = \Gamma g'(N - N_{\mathrm{tr}}),\ \tilde{n}_N(N) = \tilde{n}_0 + \frac{\alpha_{\mathrm{H}}\,g(N)}{2k_0}. \tag{6}$$

The evolution of the carrier density $N(z,t)$ in the gain section is modeled by a rate equation given in the form

$$\partial_t N = \frac{I}{qd W L_1} - \left(AN + BN^2 + CN^3\right)$$
$$-\frac{c_0}{n_g}\Re\sum_{\nu=\pm}\langle E^{\nu*}\left[g(N) - \mathcal{D}\right]E^\nu\rangle_a, \tag{7}$$
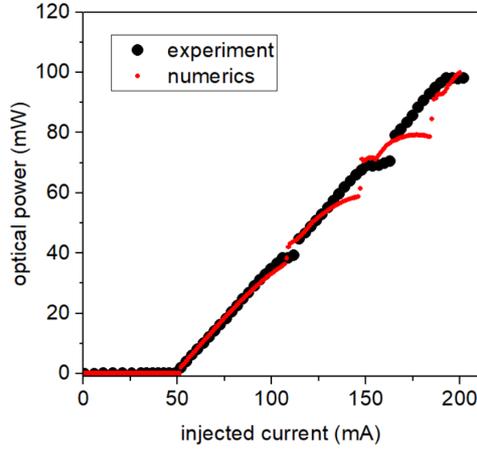
Fig. 2 – Output power *versus* injection current characteristics. Black symbols - measurement. Red symbols - simulation. Device parameters: transmission coefficient $T = 0.85$, rear facet reflectivity $R_r = 0$, front facet reflectivity $R_f = 0.3$.

where A, B, C are carrier recombination parameters. The effective width of the ridge of the RW of the gain chip is $W = 9$ μm. The ECDLs operates at $\lambda_0 = 0.87$ μm. The lengths of the sections are $L_1 = 2$ mm, $L_2 = 7$ mm, and $L_{\text{VHBG}} = 5.7$ mm. Other parameters are $c_T = 1.5 \cdot 10^5$ A^{-1}m^{-1}, $N_{\text{tr}} = 2.2 \cdot 10^{24}$ m^{-3}, $g' = 1100 \cdot 10^{-21}$ m^2, $A = 0.25 \cdot 10^8$ s^{-1}, $B = 1.0 \cdot 10^{-16}$ m^{3}s^{-1}, $C = 2 \cdot 10^{-42}$ m^{6}s^{-1}, $n_{\text{g}} = 3.9$. Values of the varying parameters are given in the captions of the figures of the paper. For more details on the model and a description of the parameters see [12] and [13].

3. RESULTS AND DISCUSSIONS

In what follows we use the model described by the equations (1)-(7) to study the electro-optical properties of the ECDL shown in Fig. 1. Figure 2 shows the measured and simulated mean output power collected at the front facet of the ECDL *versus* the injection current. Both in measurement and simulation a threshold current of 50 mA, a similar slope, and mode jumps, visible as kinks in the characteristics, are obtained. Figure 2 reveals an overall good agreement between the experimental and simulated characteristics.

Next we consider what is predicted to happen if the transmission coefficient T describing coupling losses in the air gap section is decreased from 0.85 to 0.5. The results of the calculated output power against injection current are shown in Fig. 3a. For $T = 0.85$ the ECDL exhibits, as mentioned earlier, a threshold current of 50 mA (see black line in Fig. 3). If the transmission coefficient decreases to $T = 0.7$, the threshold current increases to 57 mA and the slope efficiency decreases,
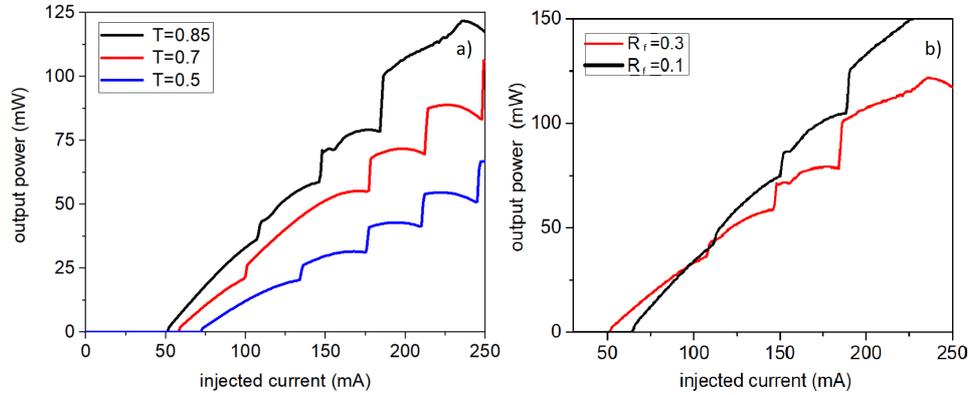
Fig. 3 – Calculated light output power *versus* injection current for different values of a) transmission coefficient ($R_f = 0.3, R_r = 0$) and b) front facet reflectivity ($R_r = 0, T = 0.85$).

as shown by the red line in Fig. 3. On the other hand, for $T = 0.7$ the mode jumps are more periodic and stable. A further decrease to $T = 0.5$ is accompanied by a further increase of the threshold current to 72 mA and a further decrease of the slope efficiency.

We discuss the influence of front facet reflectivity on the output characteristics further. Figure 3b shows the output power *versus* injection current for two values of the front facet reflectivity. When the front facet reflectivity is reduced from $R_f = 0.3$ to $R_f = 0.1$ both threshold current and slope increase, because of larger outcoupling loss and outcoupled power, respectively. The mode jumps occur at similar currents for both devices.

Let us now consider the dynamic behaviour of the ECDL. A bifurcation diagram is a very useful tool when analyzing laser dynamics. Here the injection current is considered to be the main parameter of bifurcation. In Fig. 4a continuous wave (CW) operation and several instabilities (regions U) are observed as the injection current increases above threshold. For a given value of the injection current the average power and the values of the local maximum and minimum of power are shown. At an injection current of 110 mA a Hopf bifurcation appears and the laser develops an oscillatory behavior. As the injection current rises further, the amplitude of oscillations first increases, then decreases and finally disappear in another Hopf bifurcation. A similar scenario is shown for larger injection currents. The insert in Fig. 4a shows a time trace of the output power for 200 mA injection current. One can see quasi-periodic oscillations. It can be stated that for this set of parameters ($T = 0.85$, $R_r = 0$, $R_f = 0.3$) the laser exhibits a complex behavior.

The instability regions in Fig. 4a are correlated with regions of a small side mode suppression ratio (see panel b) of Fig. 4) defined as the ratio between the
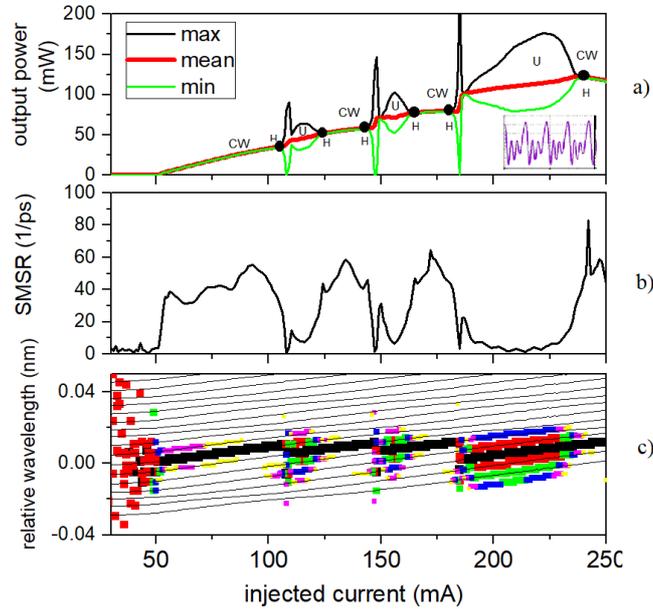
Fig. 4 – (Color online) Electro-optical characteristics of the ECDL for $T = 0.85$, $R_r = 0$, $R_f = 0.3$. a) Averaged mean (red), maximal (black), and minimal (green) output power. CW - continuous wave operation. U - unstable regions. H - Hopf bifurcations. b) Side mode suppression ratio (SMSR) obtained from the optical spectra. c) Wavelengths of the main peaks of the optical spectra (bullets) and modes of the point spectrum (thin lines). Big black bullets show the strongest optical mode. The smaller red, green, blue, violet, and beige bullets represent the side modes suppressed by less than 10, 20, 30, 40, and 50 dB, respectively. Insert in a) shows the time trace of the output power for an injection current of 200 mA.

optical power at the front facet associated with the strongest and the second strongest component of the optical spectrum (obtained by a Fourier transformation of time trace of the outcoupled optical field). The bullets in panel c) of Fig. 4 show the peak wavelengths of the optical spectrum. The size and the color of the bullets represent different levels of side mode suppression. Whereas the full black dots correspond to the strongest mode, the red, green, blue, violet, and beige bullets show the side modes suppressed by less than 10, 20, 30, 40, and 50 dB, respectively. The thin curves indicate the wavelengths of the optical modes calculated from the point spectrum of the related spectral problem of (1) constructed for the last instantaneous value of the carrier density [13]. The wavelengths determined from the peaks of the optical spectrum lie mostly on or nearby these lines.

In order to achieve a controllable stable single mode operation, one needs to improve the mode selection, which, for example, can be achieved by introducing a stronger damping in the cavity. *i.e.* a reduction of the transmission coefficient that

is analyzed in what follows. Figure 5 shows characteristics similar as in Fig. 4 for transmission coefficients $T = 0.7$ (left) and $T = 0.5$ (right). The reduction of T leads to enhanced stability in the power-current characteristics, see panel a) of Fig. 5, which is also confirmed by a large SMSR, see panel b). One can see in panel c) of Fig. 5 a nearly complete suppression of the modes that are not directly involved in the state transition where the other color bullets are almost absent in the FT spectrum. However, the decrease of the transmission coefficient T results not only in a more stable laser operation, but is also accompanied by a reduction of the output power.
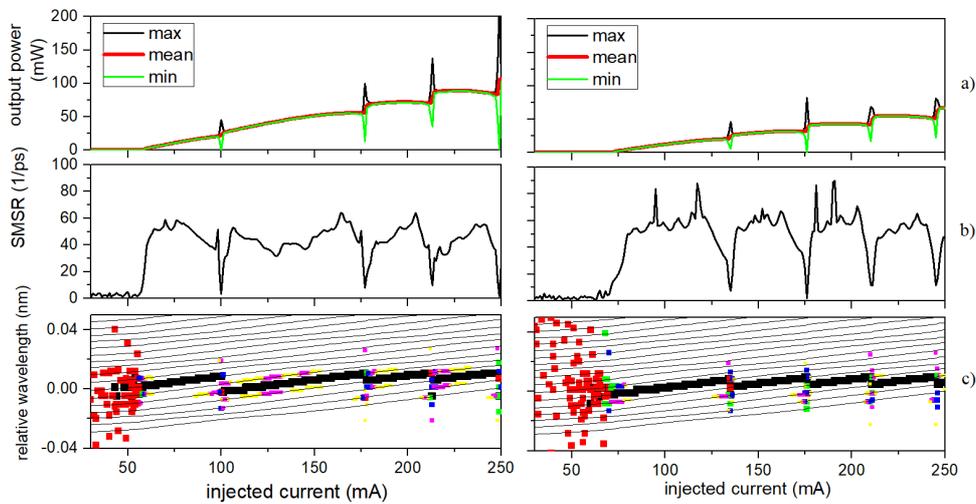

Fig. 5 – Same as Fig. 4 for different values of transmission coefficient $T = 0.7$ (left) and $T = 0.5$ (right). Other parameters: $R_r = 0, R_f = 0.3$.

In all figures above, $R_r = 0$ was assumed. In what follows, we consider the influence of a non-vanishing rear facet reflectivity R_r on the laser output characteristics. Figure 6 shows the results of a simulation for a rear facet reflectivity $R_r = 0.1$, $T = 0.85$, $R_f = 0.3$. As the injection current increases a series of instabilities appears in the power-current characteristics (see Fig. 6a), including many jumps between CW and unstable states. This unstable behaviour is also confirmed by the strongly varying SMSR shown in panel b) and the large number of colored bullets in panel c) indicating the existence of many competing modes. Thus, to achieve stable operation one needs to reduce as much as possible the reflectivity of the rear facet of the laser chip. We believe that the work presented in this paper provides a good basis for future studies to improve the experimental characteristics of ECDL devices.
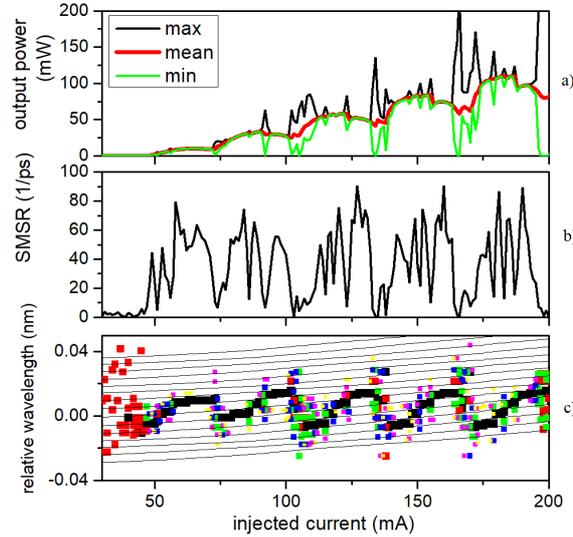
Fig. 6 – Same as Fig. 4 for $R_r = 0.1$.

4. SUMMARY

We have carried out theoretical investigations on the electro-optical performance and dynamic stability of an ECDL operating at $\lambda_0 = 0.87\mu$m. A traveling wave model coupled with a rate equation for the carrier density was used to describe the dynamic behavior of the ECDLs and to predict the dependence of the optical power, wavelength, and side mode suppression ratio in dependence on the injection current. A good agreement was obtained between measurement and simulation of the dependence of output power on the injection current for a sample device. It has been shown that to achieve a controllable stable single mode operation, one needs to reduce the transmission coefficient. However, the reduction of transmission coefficient leads to a lower output power. Finally, most stable operation is obtained for vanishing rear facet reflectivity.

REFERENCES

1. B. J. Bloom *et al.*, *An optical lattice clock with accuracy and stability at the* 10^{-18} *level*, Nature **506**, 71 (2014).
2. Z. Sodnik, B. Furch, and H. Lutz, *Optical intersatellite communication*, IEEE J. Sel. Topics Quan-

tum Electron. **16**, 1051 2010.

3. K. Bongs *et al.*, *Development of a strontium optical lattice clock for the SOC mission on the ISS*, C. R. Phys. **16**, 553–564 (2015).

4. M. Schmidt *et al.*, *A mobile high-precision absolute gravimeter based on atom interferometry*, Gyrosc. Navig. **2**, 170–177 (2011).

5. T. Schuldt, *Design of a dual species atom interferometer for space*, Exp. Astron. **39**, 167–206 (2015).

6. E. Luvsandamdin *et al.*, *Development of narrow linewidth, microintegrated extended cavity diode lasers for quantum optics experiments in space*, Appl. Phys. B **111**, 255 (2013).

7. C. Kürbis *et al.*, *Extended cavity diode laser master-oscillator-power-amplifier for operation of an iodine frequency reference on a sounding rocket*, Appl. Opt. **59**, 253–262 (2020)

8. B. Krauskopf and D. Lenstra, *Fundamental issues of nonlinear laser dynamics*, AIP Conf. Proc., volume 548, 2000.

9. R. Lang and K. Kobayashi, *External optical feedback effects on semiconductor injection laser properties*, IEEE J. Quantum Electron. **16**, 347 (1980).

10. V. Z. Tronciu, H.-J. Wünsche, M. Wolfrum, and M. Radziunas, *Semiconductor laser under resonant feedback from a Fabry-Perot resonator: Stability of continuous-wave operation*, Phys. Rev. E **73**, 046205 (2006).

11. V. Z. Tronciu *et al.*, *Chaos generation and synchronization using an integrated source with an air gap*, IEEE J. Quantum Electron. **46**, 1840 (2010).

12. M. Radziunas, V. Z. Tronciu, E. Luvsandamdin, C. Kürbis, A. Wicht, and H. Wenzel, *Study of Microintegrated External-Cavity Diode Lasers: Simulations, Analysis, and Experiments*, IEEE J. Quantum Electron. **51**, 2000408 (2015).

13. M. Krüger *et al.*, *Improving the spectral performance of extended cavity diode lasers using angled-facet laser diode chips*, Appl. Phys. B **125**, 66 (2019).

14. A. D. Ludlow, M. M. Boyd, Jun Ye, E. Peik, and P. O. Schmidt, *Optical atomic clocks*, Rev. Mod. Phys. **87**, 637 (2015).

15. U. Bandelow, M. Radziunas, J. Sieber, and M. Wolfrum, *Impact of gain dispersion on the spatio-temporal dynamics of multisection lasers*, IEEE J. Quantum Electron. **37**, 183 (2001).

16. M. Spreemann, M. Lichtner, M. Radziunas, U. Bandelow, and H. Wenzel, *Measurement and simulation of distributed-feedback tapered master-oscillator power amplifiers*, IEEE J. Quantum Electron. **45**, 609 (2009).